remote sensing

MDPI

Article

Prediction of Sea Surface Chlorophyll-a Concentrations Based on Deep Learning and Time-Series Remote Sensing Data

Lulu Yao [1,2], Xiaopeng Wang [1], Jiahua Zhang [1,2,*], Xiang Yu [1], Shichao Zhang [1] and Qiang Li [1]

[1] Remote Sensing Information and Digital Earth Center, College of Computer Science and Technology, Qingdao University, Qingdao 266071, China; 2021023957@qdu.edu.cn (L.Y.); wxp@qdu.edu.cn (X.W.); 2020010031@qdu.edu.cn (X.Y.); 2021010034@qdu.edu.cn (S.Z.); chucklee@qdu.edu.cn (Q.L.)

[2] Key Laboratory of Digital Earth Science, Aerospace Information Research Institute, Chinese Academy of Sciences, Beijing 100094, China

* Correspondence: zhangjh@radi.ac.cn; Tel.: +86-10-8217-8122

Abstract: Accurate prediction of future chlorophyll-a (Chl-a) concentrations is of great importance for effective management and early warning of marine ecological systems. However, previous studies primarily focused on chlorophyll-a inversion and reconstruction, while methods for predicting Chl-a concentrations remain limited. To address this issue, we adopted four deep learning approaches, including Convolutional LSTM Network (ConvLSTM), Convolutional Neural Network-Long Short-Term Memory (CNN-LSTM), Eidetic 3D LSTM (E3D-LSTM), and Self-Attention ConvLSTM (SA-ConvLSTM) models, to predict Chl-a over the Yellow Sea and Bohai Sea (YBS) in China. Furthermore, 14 environmental variables obtained from the remote sensing data of Moderate-resolution Imaging Spectroradiometer (MODIS) and ECMWF Reanalysis v5 (ERA5) were utilized to predict the Chl-a concentrations in the study area. The results showed that all four models performed satisfactorily in predicting Chl-a concentrations in the YBS, with SA-ConvLSTM exhibiting a closer approximation to true values. Furthermore, we analyzed the impact of the Self-Attention Memory Module (SAM) on the prediction results. Compared to the ConvLSTM model, the SA-ConvLSTM model integrated with the SAM module better captured subtle large-scale variations within the study area. The SA-ConvLSTM model exhibited the highest prediction accuracy, and the one-month Pearson correlation coefficient reached 0.887. Our study provides an available approach for anticipating Chl-a concentrations over a large area of sea.

Keywords: chlorophyll-a; remote sensing; RNNs; SA-ConvLSTM model; Yellow Sea and Bohai Sea

Citation: Yao, L.; Wang, X.; Zhang, J.; Yu, X.; Zhang, S.; Li, Q. Prediction of Sea Surface Chlorophyll-a Concentrations Based on Deep Learning and Time-Series Remote Sensing Data. *Remote Sens.* **2023**, *15*, 4486. https://doi.org/10.3390/rs15184486

Academic Editors: Zhe-Wen Zheng and Jiayi Pan

Received: 7 July 2023
Revised: 30 August 2023
Accepted: 3 September 2023
Published: 12 September 2023

1. Introduction

The ocean is a critical ecosystem, and good water quality is essential for its sustainable development [1]. Unfortunately, in recent years, water pollution has emerged as a prevalent and pressing global environmental problem [2]. The eutrophication of water bodies is a rising concern, particularly in coastal regions where the proliferation of various harmful algal species is becoming increasingly common. Chlorophyll-a (Chl-a) is a photosynthetic pigment required for phytoplankton survival. This biochemical marker has gained significance as an indicator of water eutrophication due to its abundance in most algal species [2–6]. Due to the low water exchange capacity of the Yellow Sea and Bohai Sea (YBS), red tides occur frequently, disturbing the natural balance of the local ecosystem [6–8]. It is thus crucial to monitor Chl-a concentrations in the YBS, particularly near their coasts. Developing accurate long-term Chl-a prediction strategies is vital to address coastal seawater pollution and provide timely red tide warnings.

Traditional Chl-a measurement methods using fixed-point profiles have limitations as they only target small areas, like rivers and lakes, or survey Chl-a relationships within a narrow temporal window [9–12]. Since the successful launch of the Coastal Zone Color

Scanner (CZCS), satellite remote sensing technology has played a significant role in observing global environmental changes [13]. Satellite-based remote sensing provides larger-scale and higher-resolution data, creating novel opportunities for predicting and estimating sea surface Chl-a concentrations [14]. Many remote sensing data are open-source and readily available, reducing the cost of scientific investigation. The utilization of satellite data enables the close monitoring of Chl-a concentrations, red tides, and other related phenomena, facilitating timely warning and response [15].

The dynamics of algal biomass are nonlinear and nonstationary due to complex interactions among physical, chemical, and biological parameters [11,16]. Vollenweider et al. [17] developed a basic mass balance and export model to represent the eutrophication of lakes. However, this model failed to account for other relevant environmental factors. In contrast, Jørgensen et al. [18] established a eutrophication model based on water body properties, but determining the optimal water quality parameters remained challenging. Scholars attempt to employ the autoregressive integrated moving average (ARIMA) model in order to address the forecasting challenges associated with discrete time series [19]. However, ARIMA is best suited for linear, seasonal, or stable data, which has great limitations. With the development of the big data era, the field of remote sensing has also used computer technology to solve problems [1]. Machine learning can solve complex problems that are difficult with traditional methods. Deep learning is a special machine learning, which has been applied to the marine field in recent years, such as predicting sea surface temperature [20], wave height [21], and sea surface Chl-a concentrations [12,22–24]. Many current research efforts have successfully predicted Chl-a using machine learning models, including Random Forest (RF) [12], Support Vector Regression (SVR) [23], Convolutional Neural Networks (CNN) [24,25], and Recurrent Neural Networks (RNN) [26]. Especially, RNN can produce higher accuracy for temporal data prediction and obtain the temporal and spatial characteristics of the data, so RNN and its variant Long Short-Term Memory Neural Network (LSTM) are more widely applied to the prediction of temporal data [9,10,20,24,26].

With the development of computer technology, there are many improved models for time series data prediction. The internal structure of Convolutional LSTM Network (ConvLSTM) [27] takes spatial features into account; Recurrent Neural Networks for Predictive Learning (PredRNN) [28] and PredRNN++ [29] models enhance the long-term and short-term memory of data. Eidetic 3D LSTM (E3D-LSTM) [30] and Self-Attention ConvLSTM (SA-ConvLSTM) [31] introduce the idea of attention mechanism; they focus on the spatial and temporal characteristics of the data. These models have achieved good results in video prediction and can be more widely used in other time series data prediction fields [20,21,32–35]. Liu et al. [22] used Convolutional Neural Network-Long Short-Term Memory (CNN-LSTM) for an effective three-year long-term prediction of Chl-a concentrations in the South China Sea. Ahmed et al. [26] used multiple deep learning models for the estimation of optically active parameters. The results show that the LSTM model takes into account the temporal dependence of the data and solves the problem of gradient disappearance compared to the traditional RNN. Most previous studies have relied on historical data of Chl-a to predict the future Chl-a, with insufficient consideration given to the impact of environmental variables [22,24]. Furthermore, prior research on Chl-a prediction suffers from the problems of single research data and imprecise spatial scales as it relies on decreasing the resolution of the data by resampling to achieve predictions for large areas of the sea.

This study takes advantage of the high frequency and wide coverage of satellite observations and the ability of deep learning to reveal nonlinear relationships among data to estimate and predict Chl-a concentrations for one month in the YBS. A variety of deep learning models, including ConvLSTM, CNN-LSTM, E3D-LSTM, and SA-ConvLSTM, are trained to predict the Chl-a concentrations while maintaining the original spatial resolution of the sea surface in the YBS. Furthermore, 19 years of Moderate-resolution Imaging Spectroradiometer (MODIS) satellite remote sensing data and the ECMWF Reanalysis v5 (ERA5) dataset from 2003 to 2021, including sea surface temperature (SST), sea waves, wind,

particulate organic carbon (POC), surface pressure (SP), and other variables, are used to predict the Chl-a concentrations. Furthermore, the influence of the Self-Attention Memory Module (SAM) on the predictive performance of the SA-ConvLSTM model is analyzed.

2. Materials and Methods

2.1. Study Area

The study area is located in the YBS, in the northern part of China, a semi-enclosed sea area (Figure 1). Map data are derived from the Natural Earth [36] and OceanColor [37]. This geography allows for long water renewal times, slow circulation of harmful algae and other pollutants, and long retention times in the YBS [6,7]. The dataset covers the area bounded by 32–45°N and 114–127°E, as shown in blue on the map. The YBS have a complex biochemical environment and large-scale phytoplankton distribution. As many rivers flowing into the YBS pass through industrial and agricultural areas, they carry a variety of nutrients. The aquaculture industry in the YBS is flourishing, and the eutrophication of the offshore waters has been serious in recent decades because of the influence of human activities, with frequent outbreaks of harmful algal blooms [2,3,38]. It is important to monitor and predict the sea surface Chl-a for the ecological development of the YBS [39].

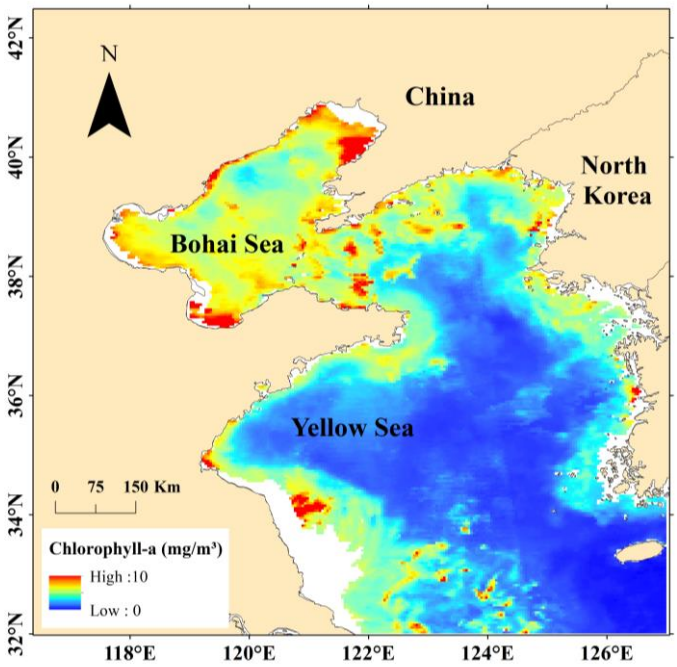

Figure 1. The location of the study area. The chlorophyll-a data shown in the figure represent the data for May 2021, with the white areas indicating missing values.

2.2. Dataset

Phytoplankton growth is influenced by a multifaceted interplay of physical, chemical, and biological factors [11,16]. There is a robust correlation between SST and Chl-a concentrations [40]. The interaction between POC, particulate inorganic carbon (PIC), and Chl-a reflects the productivity and carbon cycle process of marine ecosystems [41,42]. Photosynthetically available radiation (PAR) exhibits a strong positive correlation with Chl-a [42]. The distribution of phytoplankton can be influenced by ocean physical processes, such as wind-induced upwelling [43]. Therefore, the 10 m zonal and meridional winds (U10 and V10) can serve as predictors for Chl-a estimation. In oligotrophic or eutrophic water bodies, phosphorus has a stronger influence on Chl-a levels [44]. Xing et al. [3] reconstructed daily MODIS Chl-a concentrations in the northwestern Pacific using SST, T2M, MSL, U10, V10, and other parameters. This study attempted to consider as many environmental factors in the YBS as possible using all available data. This work used a wide range of environmental

factors, including physical, chemical, and biological parameters, such as 2 m temperature (T2M), U10, V10, SP, total precipitation (TP), mean sea level pressure (MSL), significant height of combined wind waves and swell (SWH), mean wave direction (MWD), and mean wave period (MWP). Detailed parameters are shown in Table 1.

Table 1. Training, validation, and testing datasets used to develop the model of Chl-a prediction.

Parameter	Description	Unit	Spatial Resolution	Temporal Resolution	Data Source
Chl-a	Chlorophyll-a Concentrations	mg/m^3	4 km × 4 km	Monthly	OceanColor
PIC	Particulate Inorganic Carbon	mol/m^3			
POC	Particulate Organic Carbon	mol/m^3			
SST	Sea Surface Temperature	degree_C			
PAR	Photosynthetically Available Radiation	$einstein/m^2/day$			
NFLH	Normalised Fluorescence Line Height	$W/m^2/um/sr$			
U10	10 Metre U Wind Component	m/s	0.25° × 0.25°	Monthly	ERA5
V10	10 Metre V Wind Component	m/s			
T2M	2 Metre Temperature	K			
SP	Surface Pressure	Pa			
TP	Total Precipitation	m			
MSL	Mean Sea Level Pressure	Pa	0.5° × 0.5°	Monthly	ERA5
SWH	Significant Height of Combined Wind Waves and Swell	m			
MWD	Mean Wave Direction	Degree	1° × 1°	Monthly	ERA5
MWP	Mean Wave Period	s			

The satellite data are adopted for both monitoring and prediction of Chl-a concentrations. The data time series is about 19 years (from January 2003 to December 2021) with monthly temporal resolution. OceanColor data are from MODIS L3 level data. The data are provided by NASA and can be downloaded from this open site (https://oceancolor.gsfc.nasa.gov, accessed on 16 May 2022) at the spatial resolution of 4 km. Climate data are from the ERA5 meteorological reanalysis data (https://cds.climate.copernicus.eu, accessed on 16 May 2022). The spatial resolution of meteorological data is not the same. The spatial resolution of reanalysis data is 0.25°, and the parameters of uncertainty estimation are 0.5° and 1°. To establish a comprehensive dataset for Chl-a, it is necessary to unify the spatial resolution of remote sensing data using a linear interpolation method.

In this paper, the directly downloaded satellite remote sensing data are called true data. The training data used by the model, that is, true label, are the data of true data after data preprocessing. The spatial resolution of the two remote sensing datasets is different. Since Chl-a is used as the target parameter, the spatial resolution of ERA5 data is resampled to 4 km. Remote sensing data are susceptible to missing values due to weather, satellite malfunctions, and other reasons. In this study, we employed DINEOF to fill in the missing values for each variable [4,45]. Next, negative pixel masking was used to remove abnormally negative values of Chl-a. Meteorological data include land and ocean, and there will be outliers in the land part of ocean water color data, so it is necessary to mask the land. Finally, all variables were masked to exclude land data. Data are not comparable because of different dimensions, which can be eliminated after normalization. This study adopted Min–Max normalization [23,46].

Before model training, the dataset of about 19 years (from January 2003 to December 2021) needs to be divided. In terms of the time dimension, the dataset is separated into training set, validation set, and testing set according to the ratio of 70%, 15%, and 15%. Specifically, the training set consists of 156 months spanning from January 2003 to December 2015, the validation set comprises 36 months from January 2016 to December 2018, and the testing set includes 36 months ranging from January 2019 to December 2021. Among them, 156,36 and 36 are the timescales of the training set, the validation set, and the testing

set, which contain satellite images of all features over 156, 36, and 36 months, respectively. Each image contains a great deal of information and samples. Due to the resolution being 4 km × 4 km, each image contains 312 × 312 pixels. We predicted Chl-a concentrations of each pixel.

2.3. Methods

2.3.1. Deep Learning Models and Implementation

This study used a variety of deep learning models to compare the monitoring and prediction effects of Chl-a by training ConvLSTM, CNN-LSTM, E3D-LSTM, and SA-ConvLSTM models. CNN is often used in classification and segmentation, which can extract features well [47,48]. However, for the prediction of time series, RNN and LSTM have a good effect compared with CNN [23,26]. The CNN-LSTM model, which directly connects CNN and LSTM in series, cannot only provide excellent feature extraction ability of CNN but also consider the correlation of data in time dimension [10,22]. ConvLSTM is a variant of LSTM that allows data to be held in both time and space. Both E3D-LSTM and SA-ConvLSTM add attention mechanism [49], E3D-LSTM strengthens the long-distance dependence ability of LSTM, and SA-ConvLSTM solves the long-term spatial dependence problem [30,31,50]. Four networks were trained with varying parameter magnitudes to comprehensively evaluate the impact of model complexity on Chl-a prediction.

1. ConvLSTM

In this study, a total of four ConvLSTM [27] layers are stacked. Each layer in the stack comprised a standard ConvLSTM, which consisted of three components: the forget gate, the input gate, and the output gate. In addition, ReduceLROnPlateau was adopted to optimize the learning rate [51]. ReduceLROnPlateau was a method to dynamically adjust the learning rate according to indicators. The strategy chosen in this study was to automatically adjust the learning rate when the verification loss was no longer reduced.

2. CNN-LSTM

Unlike previous studies that proposed a CNN-LSTM model [22,52], we developed a novel CNN-LSTM architecture in this study. The introduction of 2D convolutions and the deconvolutional layer into the CNN-LSTM model has enhanced the ability of the model to capture local features and spatial information. CNN-LSTM is a network that combines the advantages of CNN and LSTM models, including six parts: convolutional layer, pooling layer, deconvolution layer, flattening layer, LSTM layer, and output layer. The network structure is shown in Figure 2. In the early stage, CNN was used to extract deep features, the ReLU activation function was used to add nonlinear factors to improve model expression ability, and batch normalization was used to alleviate the overfitting problem [53]. Due to insufficient training samples, introducing L2 regularization to reduce overfitting can also increase the generalization ability of the model [54]. LSTM has good performance for time series data. In this study, we leveraged the power of LSTM to capture temporal dependencies within the data, ultimately using a fully connected layer to output the predicted Chl-a values.

3. E3D-LSTM

By combining 3D convolution with RNNs, the E3D-LSTM model can capture both long-term dependencies in time and store short-term features, leading to improved prediction performance [30]. To comprehensively capture the spatiotemporal characteristics of the YBS, the E3D-LSTM model was developed in this study to predict Chl-a concentrations. The E3D-LSTM uses the Encoder–Decoder framework, which consists of a 4-layer E3D-LSTM encoder and a layer of 3D CNN decoder. E3D-LSTM incorporates an attention mechanism based on the spatiotemporal LSTM proposed in PredRNN [28], which improves its long-term memory capacity and enables it to capture spatiotemporal dependencies in the data. This is the first time that the E3D-LSTM model has been applied to predict sea surface Chl-a concentrations.

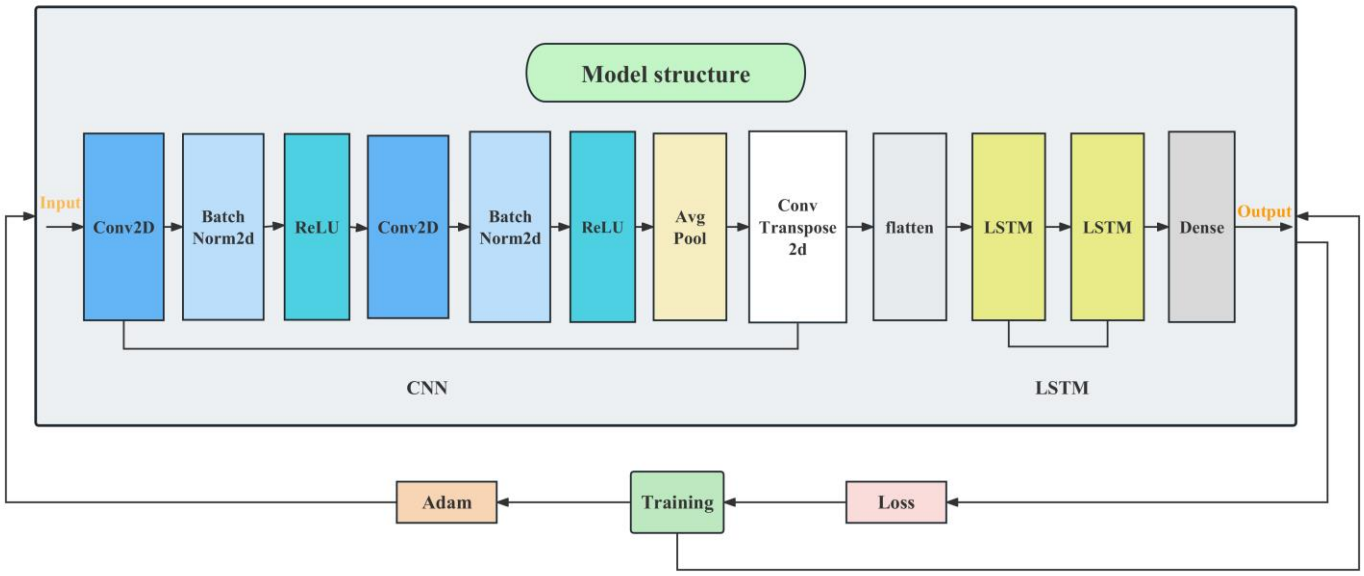

Figure 2. The CNN-LSTM network structure diagram.

4. SA-ConvLSTM

SA-ConvLSTM consists of four parts: three gates and the attention module SAM. If the SAM is removed and the forget gate, input gate, and output gate are kept, this structure is the standard ConvLSTM. The internal structure diagram of the SA-ConvLSTM network is shown in Figure 3. While ConvLSTM builds upon the LSTM architecture by replacing dot multiplication with a convolution operation to enable simultaneous attention to spatial and temporal data, relying solely on the convolution operation is insufficient for capturing the complex relationships within the current space. Incorporating an attention mechanism allows the model to selectively focus on important aspects of the data, improving its ability to capture and learn complex patterns and relationships [49]. Since the spatial coordinates of the data at each time point are related, the SAM module is designed to capture long-term spatial dependencies and enhance the model's long-term memory [31]. SA-ConvLSTM can be expressed by the following formula:

$$\hat{X}_t = SA(X_t) \tag{1}$$

$$\hat{H}_t = SA(\hat{H}_{t-1}) \tag{2}$$

where X_t represents the input at time t, $\hat{H}_{t-1}$ represents the input state at time $t-1$, $\hat{X}_t$ and $\hat{H}_t$ represent the output at time t, and SA represents the SA-ConvLSTM processing.

$$i_t = \sigma(W_i \otimes [\hat{H}_{t-1}, X_t] + b_i) \tag{3}$$

$$f_t = \sigma(W_f \otimes [\hat{H}_{t-1}, X_t] + b_f) \tag{4}$$

$$o_t = \sigma(W_o \otimes [\hat{H}_{t-1}, X_t] + b_o) \tag{5}$$

$$g_t = \tan h(W_g \otimes [\hat{H}_{t-1}, X_t] + b_g) \tag{6}$$

$$C_t = f_t \odot C_{t-1} + i_t \odot g_t \tag{7}$$

$$\hat{H}_t = o_t \odot \tanh(C_t) \tag{8}$$

where i_t, f_t, o_t, and g_t represent the states of input gate, forget gate, output gate, and update gate at time t; C_{t-1} and C_t represent the candidate states of input gate and output gate at time $t-1$ and t; W_i, W_f, W_o, and W_g represent the weights of input gate, forget gate, output gate, and update gate, respectively. b_i, b_f, b_o, and b_g are deviation from four parts; σ and tan h are two different activation functions; $\otimes$ is the element-wise addition; $\odot$ is the element-wise product.

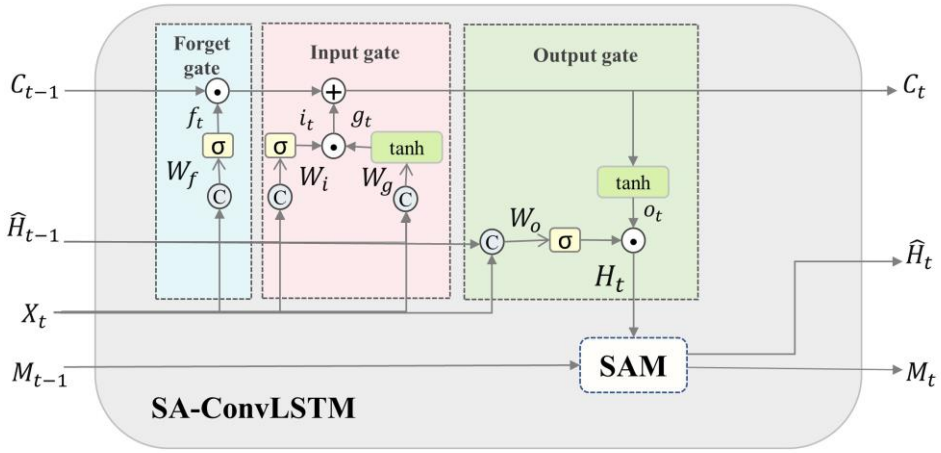

Figure 3. SA-ConvLSTM network structure diagram.

However, introducing a new module inevitably increases the complexity of the model. Complex network structures and large amounts of data pose challenges to limited hardware resources. To address these issues, this study employs a block-based training method, whereby the data are divided into small blocks during each training round, with the channel dimension expanded by a factor of n (where n is the number of blocks). During the final prediction phase, the image predicted by the model is integrated back to the size of the original image. This approach reduces the memory requirements for each round of training and better captures inter-block dependencies. Furthermore, this study represents the first application of the SA-ConvLSTM model to predict sea surface Chl-a concentrations.

In this study, the SA-ConvLSTM model adopts the Seq2Seq structure (Figure 4). Following parameter adjustment, the model now consists of 4 stacked layers of SA-ConvLSTM, with a total of 8 self-attention nodes and a patch size of 4. The batch size is set to 2, and a 3×3 convolution kernel is utilized within the model.

2.3.2. Computer Configuration and Parameter Settings

The loss function of the four models is MSELoss, which stands for mean squared error. The optimization function uses the Adam optimizer, which has a fast gradient descent speed and is suitable for large parameter numbers. We set epochs to 150, the initial value of the learning rate is 0.0001, and the learning rate is dynamically adjusted according to the ReduceLROnPlateau strategy until the model converges. In this study, the rolling prediction method can make up for the lack of data volume and use three months of Chl-a to predict one month of Chl-a. The model batch size needs to be selected according to the computer configuration, and the selected value is 2 for all models implemented on NVIDIA GeForce RTX3090. In addition, the model implementation is supported by the PyTorch library.

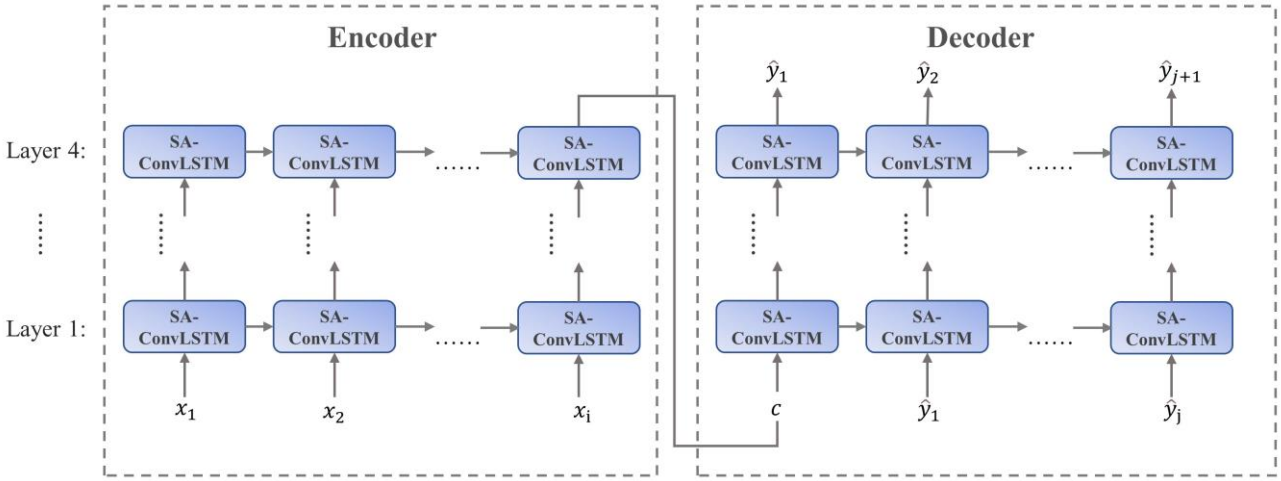

Figure 4. SA-ConvLSTM model for spatio-temporal prediction architecture. The gray arrows indicate the path of the spatio-temporal memory. Layer is a stack of SA-ConvLSTM, x_i represents the ith input of the model, and $\hat{y}_j$ is the jth output sequence of the model.

2.3.3. Evaluation Indictors

To evaluate the performance of the model, Mean Absolute Error (MAE), Mean Square Error (MSE), Root Mean Square Error (RMSE), normalized standard deviation (NSD), and Pearson correlation coefficient (r) are used [22,55]. The smaller MAE, MSE, and RMSE are, the higher the predicted Chl-a accuracy. The value of r can range from -1 to 1, with r of 0 indicating no linear relationship. r closer to either 1 or -1 indicates a stronger linear relationship. The evaluation indicators are defined as follows:

$$\mathrm{MSE} = \frac{1}{n}\sum_{i=1}^{n}(x_i - y_i)^2 \tag{9}$$

$$\mathrm{RMSE} = \sqrt{\frac{1}{n}\sum_{i=1}^{n}(x_i - y_i)^2} \tag{10}$$

$$\mathrm{MAE} = \frac{1}{n}\sum_{i=1}^{n}|x_i - y_i| \tag{11}$$

$$r = \frac{\sum_{i=1}^{n}(x_i - \overline{x})(y_i - \overline{y})}{\sqrt{\sum_{i=1}^{n}(x_i - \overline{x})^2}\sqrt{\sum_{i=1}^{n}(y_i - \overline{y})^2}} \tag{12}$$

$$\mathrm{NSD} = \frac{\sqrt{\sum_{i=1}^{n}(y_i - \overline{y})^2}}{\sqrt{\sum_{i=1}^{n}(x_i - \overline{x})^2}} \tag{13}$$

where n represents the total number of samples of Chl-a, x_i represents the true label of the ith Chl-a, y_i represents the predicted value of the ith, $\overline{x}$ represents the average of the true values of all Chl-a samples, and $\overline{y}$ represents the average of the predicted values of Chl-a.

2.3.4. Method Flow

This work can be divided into four parts: data preprocessing, model training, data prediction, and model evaluation. In the current study, 14 kinds of data from OceanColor and ERA5 are used to predict Chl-a. The Chl-a dataset is formed after preprocessing, such as study area clipping, missing value imputation, masking, and resampling. The complete Chl-a dataset is divided independently into training, validation, and testing sets. Four models (ConvLSTM [27], CNN-LSTM, E3D-LSTM [30], and SA-ConvLSTM [31]) are employed to train and predict Chl-a. The weights of the model are trained using the

training set, while the performance of the model is evaluated and compared using the validation and testing sets. The flow chart is shown in Figure 5.

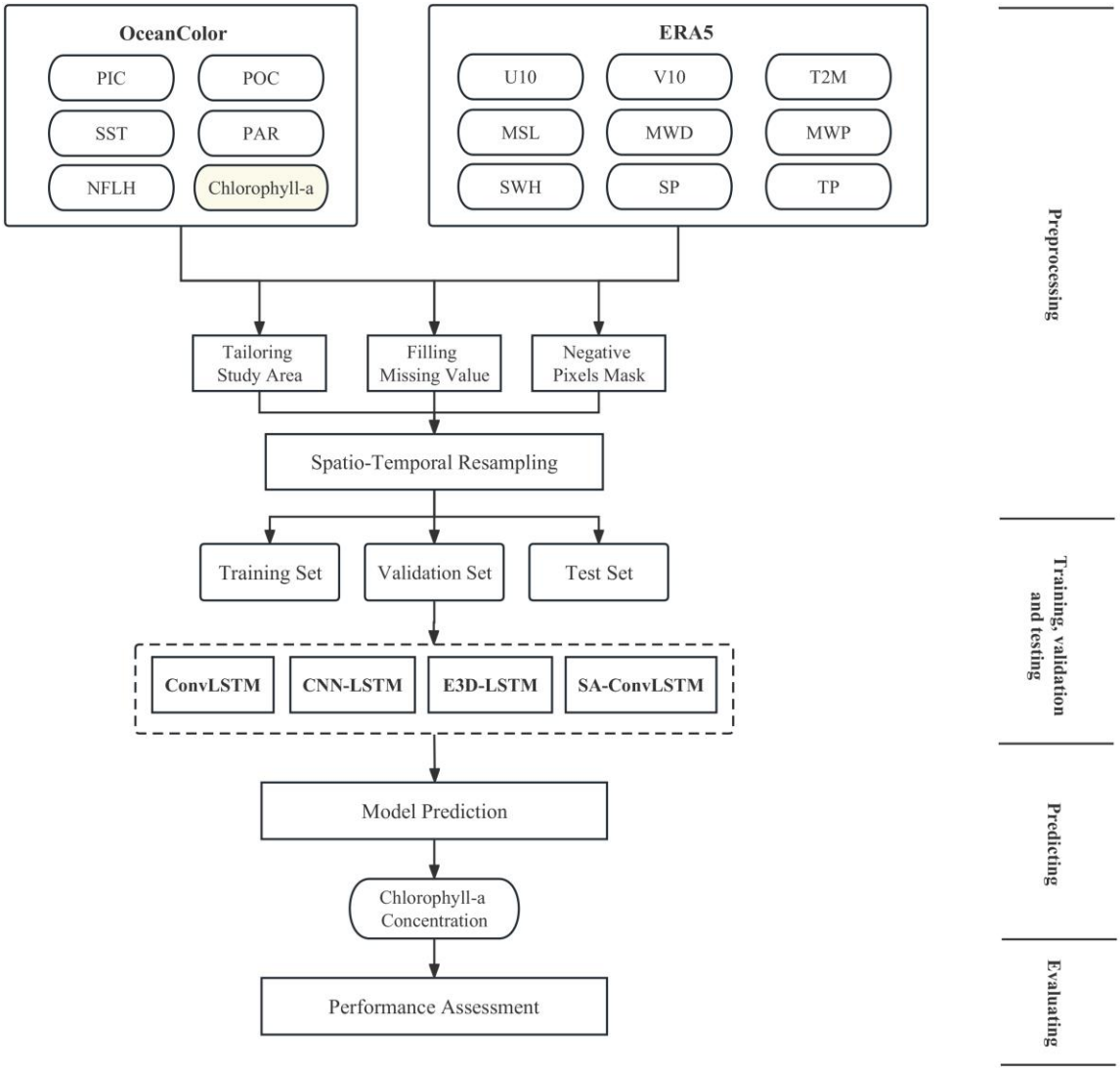

Figure 5. Flow chart of Chl-a monitoring and forecasting.

3. Results

3.1. Spatial and Temporal Evaluation of Models for Predicting Chl-a

To evaluate the prediction effect of the models and observe potential differences across various seasons, we utilized the Chl-a prediction in the YBS of the four models for different months, which are May, August, and December 2021, respectively. The original satellite data, the ground truth, and the prediction results obtained by each model are shown in Figures 6–8. The results show that the SA-ConvLSTM model demonstrated superior performance in predicting Chl-a concentrations in the YBS. Specifically, its predicted trends were highly consistent with the true labels. Meanwhile, E3D-LSTM exhibited lower accuracy than SA-ConvLSTM but still outperformed the ConvLSTM and CNN-LSTM models.

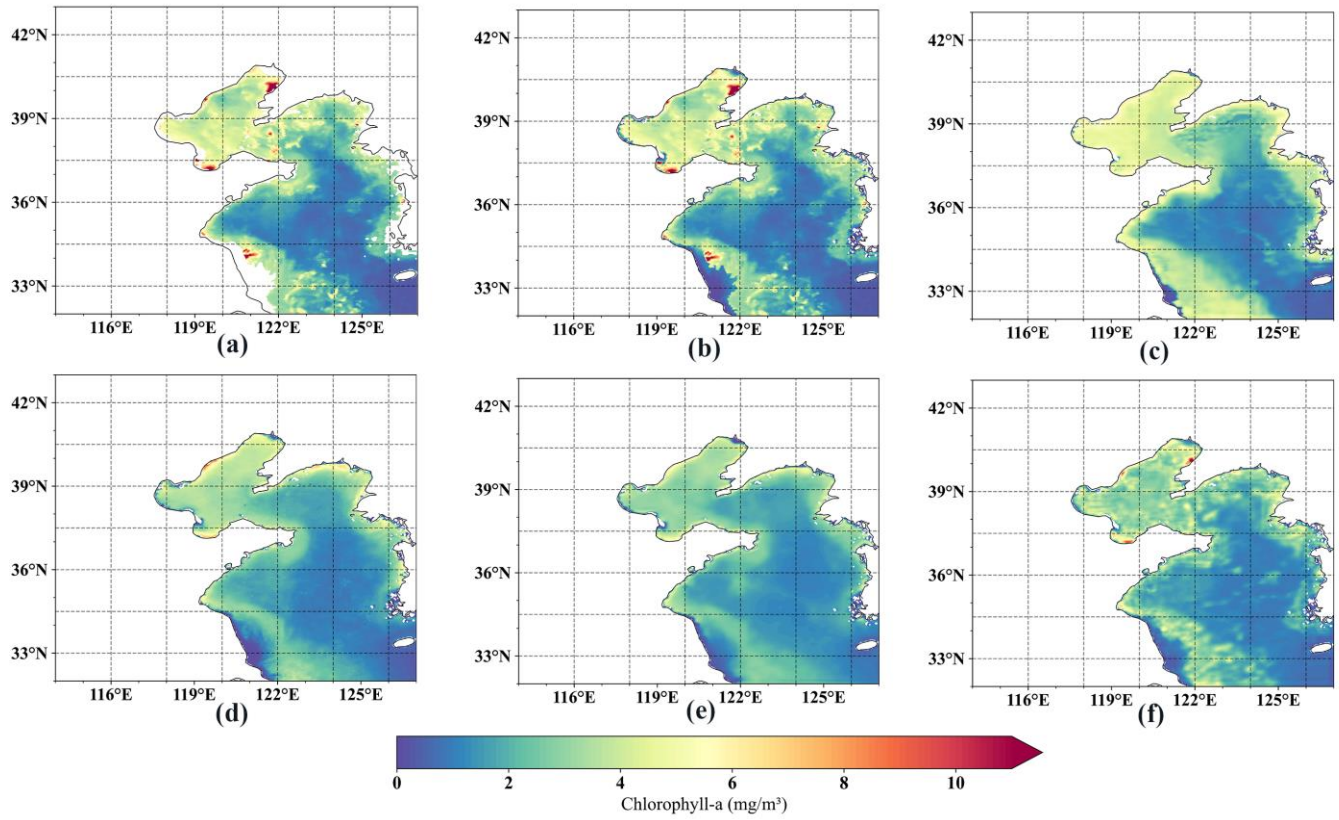

Figure 6. Comparison of four model predictions in May 2021. (**a**) The original satellite data in May 2021, (**b**) True label, (**c**) Chl-a concentrations predicted by ConvLSTM, (**d**) Chl-a concentrations predicted by CNN-LSTM, (**e**) Chl-a concentrations predicted by E3D-LSTM, and (**f**) Chl-a concentrations predicted by SA-ConvLSTM.

Notably, Figure 6 shows that the SA-ConvLSTM model demonstrated superior performance compared to other models in predicting small-scale characterizations of Chl-a concentrations. Additionally, compared to the Bohai Sea, the predicted values of Chl-a in the Yellow Sea by all three models (ConvLSTM, CNN-LSTM, and SA-ConvLSTM) were closer to the true values. As revealed in Figure 7, Chl-a concentrations gradually decreased from coastal to deep sea. The four models performed relatively well in predicting Chl-a trends in deep-sea regions, but the SA-ConvLSTM model demonstrated better performance in predicting Chl-a concentrations in nearshore areas than the other three models, which tended to underestimate the Chl-a concentrations in these regions. This trend was particularly evident in the southern Yellow Sea, where the ConvLSTM, CNN-LSTM, and SA-ConvLSTM models failed to capture the high Chl-a concentrations.

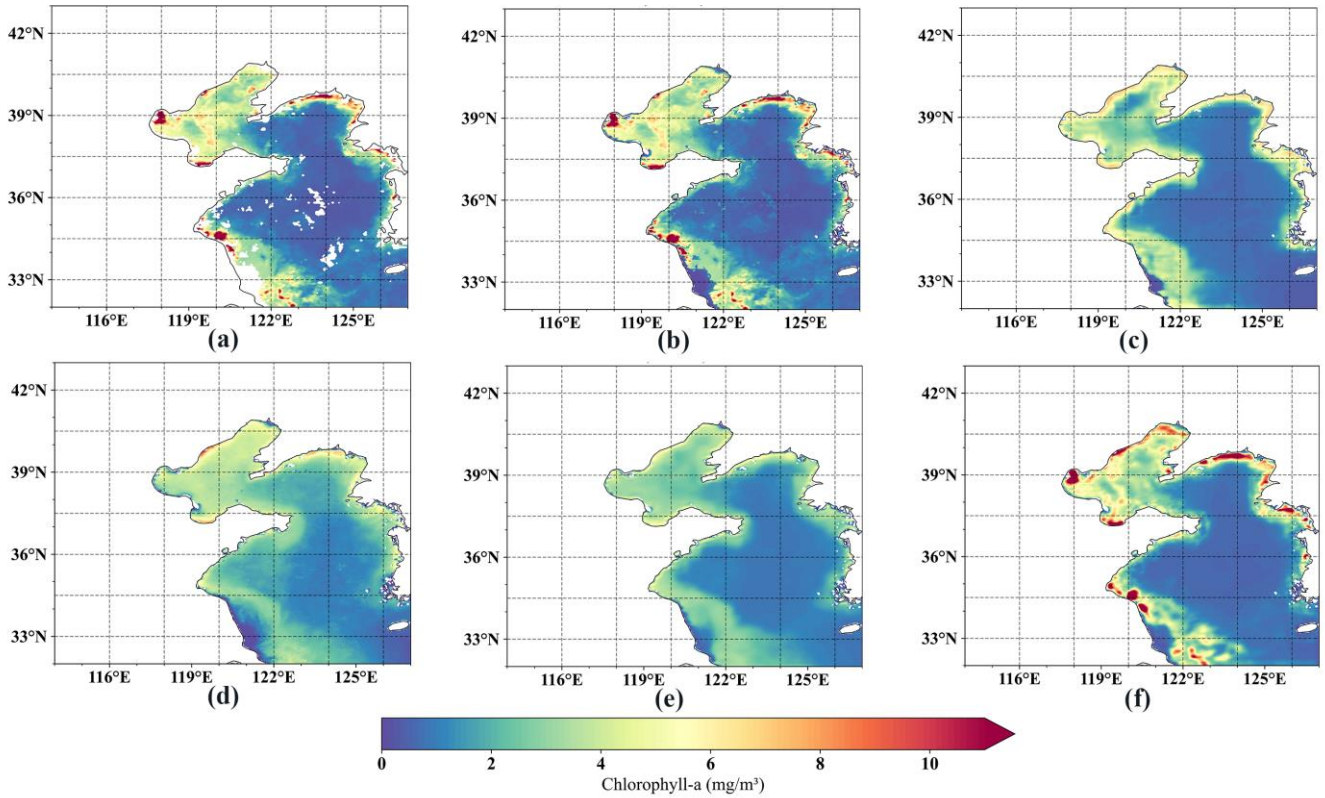

Figure 7. Comparison of four model predictions in August 2021. (**a**) The original satellite data in August 2021, (**b**) True label, (**c**) Chl-a concentrations predicted by ConvLSTM, (**d**) Chl-a concentrations predicted by CNN-LSTM, (**e**) Chl-a concentrations predicted by E3D-LSTM, and (**f**) Chl-a concentrations predicted by SA-ConvLSTM.

Furthermore, Figure 8 demonstrated that the Chl-a concentrations in the Bohai Sea were generally higher than those in the Yellow Sea. The average Chl-a concentration in the Yellow Sea in December 2021 was 2.733 mg/m^3, while the average Chl-a concentration in the Bohai Sea was 1.641 mg/m^3 higher than that in the Yellow Sea. Moreover, the four models accurately predicted Chl-a concentrations trends in the deep sea and Yellow Sea, but they showed relatively lower accuracy in the Bohai Sea coast on the Shandong Peninsula. In addition, r was used to evaluate the performance of the four models in the Yellow Sea and the Bohai Sea. The results showed that the prediction accuracy of the four models in the Yellow Sea was overall higher than in the Bohai Sea. SA-ConvLSTM had the highest accuracy of Chl-a in the Yellow Sea (r = 0.893), and the r of predicting Chl-a in the Bohai Sea reached 0.877. The prediction accuracy of ConvLSTM, CNN-LSTM, and E3D-LSTM in the Yellow Sea was 2.5%, 1.9%, and 1.8% higher than that in the Bohai Sea, respectively. Overall, despite its relatively lower accuracy in some nearshore areas, the SA-ConvLSTM, which introduced SAM, demonstrated better overall prediction performance in the YBS than other models.

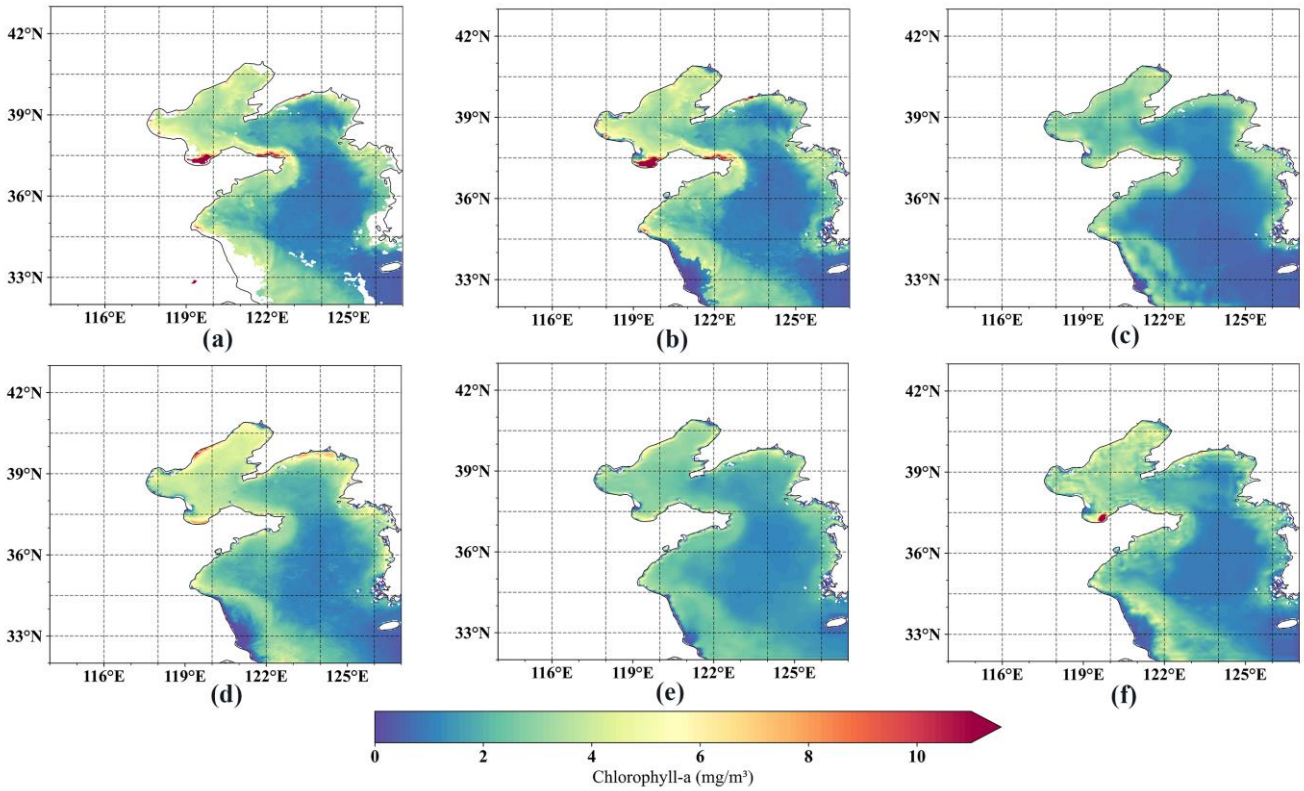

Figure 8. Comparison of four model predictions in December 2021. (**a**) The original satellite data in December 2021, (**b**) True label, (**c**) Chl-a concentrations predicted by ConvLSTM, (**d**) Chl-a concentrations predicted by CNN-LSTM, (**e**) Chl-a concentrations predicted by E3D-LSTM, and (**f**) Chl-a concentrations predicted by SA-ConvLSTM.

Figure 9 shows that the four models maintained good performance and consistency for the prediction of Chl-a concentrations in deep-sea areas. However, the ConvLSTM and CNN-LSTM models tended to overestimate Chl-a concentrations in coastal regions of the YBS while underestimating them in the Bohai Sea. The E3D-LSTM model exhibited a slight overestimation of Chl-a concentrations in the Yellow Sea and an underestimation in the Bohai Sea area. Comparing Figure 9a with Figure 9d, incorporating the SAM module allowed the SA-ConvLSTM to greatly improve prediction performance, particularly in resolving the overestimation issue encountered by the ConvLSTM model for Chl-a concentrations in coastal regions. Although SA-ConvLSTM exhibited some underestimation of Chl-a concentrations in the Bohai Sea, it demonstrated the best overall performance in the YBS.

Figure 10 shows the variation curves of Chl-a prediction results over time for ConvLSTM and SA-ConvLSTM. Compared with ConvLSTM, the tendency of SA-ConvLSTM to learn Chl-a was closer to the change in true Chl-a. After introducing the SAM module, the ability of SA-ConvLSTM to learn the future Chl-a change trend by extracting the spatiotemporal information of the data was enhanced. In this study, a significant deviation was observed between the predicted and actual values of Chl-a concentrations for July and August 2020. The discrepancy might be attributed to the varying impacts of natural and anthropogenic factors on the marine environment each year [11]. The Chl-a concentrations in the YBS exhibit intricate characteristics due to the combined effects of a complex interplay among physical, chemical, and biological factors [56]. SA-ConvLSTM and ConvLSTM showed a downward trend in the Chl-a concentrations forecast for September to October 2020 due to the deviation, with ConvLSTM being more affected. From December 2020 to June 2021, the Chl-a concentrations increased first and then decreased rapidly. Chl-a decreased rapidly after reaching its maximum values in April 2021 and slowed down

around May 2021. SA-ConvLSTM learned the trend of Chl-a, but Chl-a predicted by ConvLSTM reached its maximum values in March 2021. Similarly, from September 2021 to January 2022, the Chl-a concentrations first increased and then decreased. The changing trend in Chl-a learned by SA-ConvLSTM was consistent with the actual trend. However, ConvLSTM showed that Chl-a decreased to the minimum values and then increased during this period. In general, the tendency of SA-ConvLSTM to learn Chl-a was closer to the change in actual Chl-a.

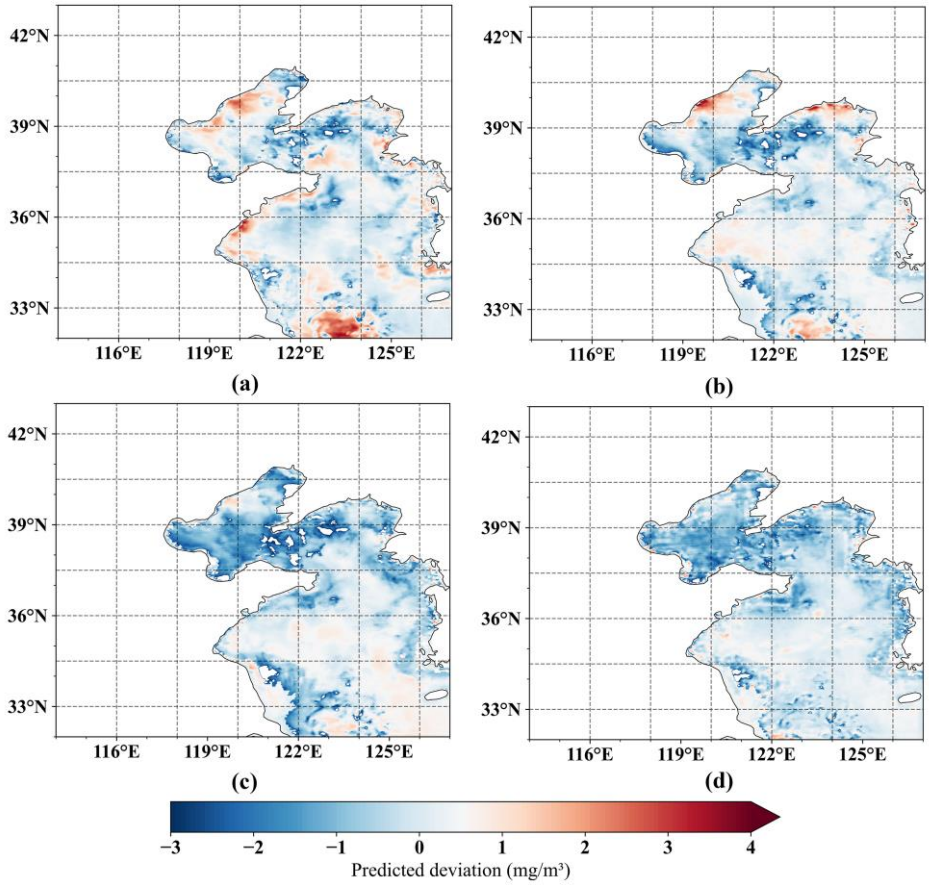

Figure 9. The predicted deviation plots of chlorophyll-a concentrations in May 2021 by different models. The predicted deviation is obtained by subtracting the actual values from the predicted values. The regions underestimated by the model are shown in blue, and the regions overestimated by the model are shown in red. (**a**) ConvLSTM, (**b**) CNN-LSTM, (**c**) E3D-LSTM, (**d**) SA-ConvLSTM.

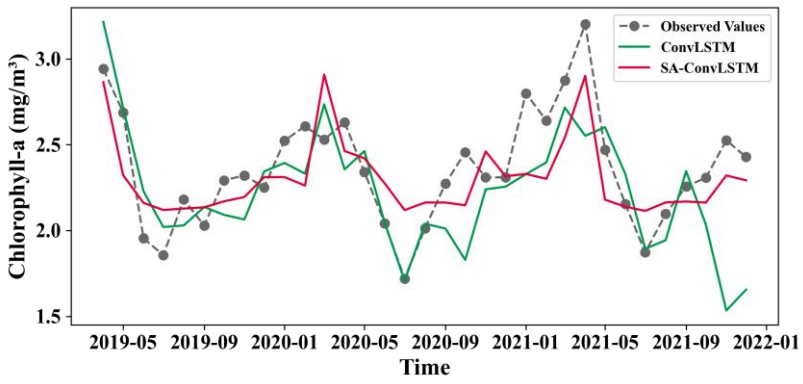

Figure 10. The trends of monthly average Chl-a in the Yellow Sea and Bohai Sea on the testing set and comparison of two model predictions.

3.2. Performance Evaluation of Models for Predicting Chl-a

Figure 11 shows the loss function plots for four models during training and validation epochs. From Figure 11, SA-ConvLSTM had the lowest training and validation losses, indicating the best performance for predicting Chl-a. Meanwhile, the CNN-LSTM model exhibited the fastest convergence speed. Although both E3D-LSTM and SA-ConvLSTM showed initial signs of convergence at around 30 epochs, E3D-LSTM took the longest time to train due to its higher model complexity among the four models. The ConvLSTM model had not fully converged even after 150 epochs of training. The validation loss for CNN-LSTM, E3D-LSTM, and SA-ConvLSTM remained consistently lower than the training loss, indicating that these three models demonstrated neither underfitting nor overfitting.

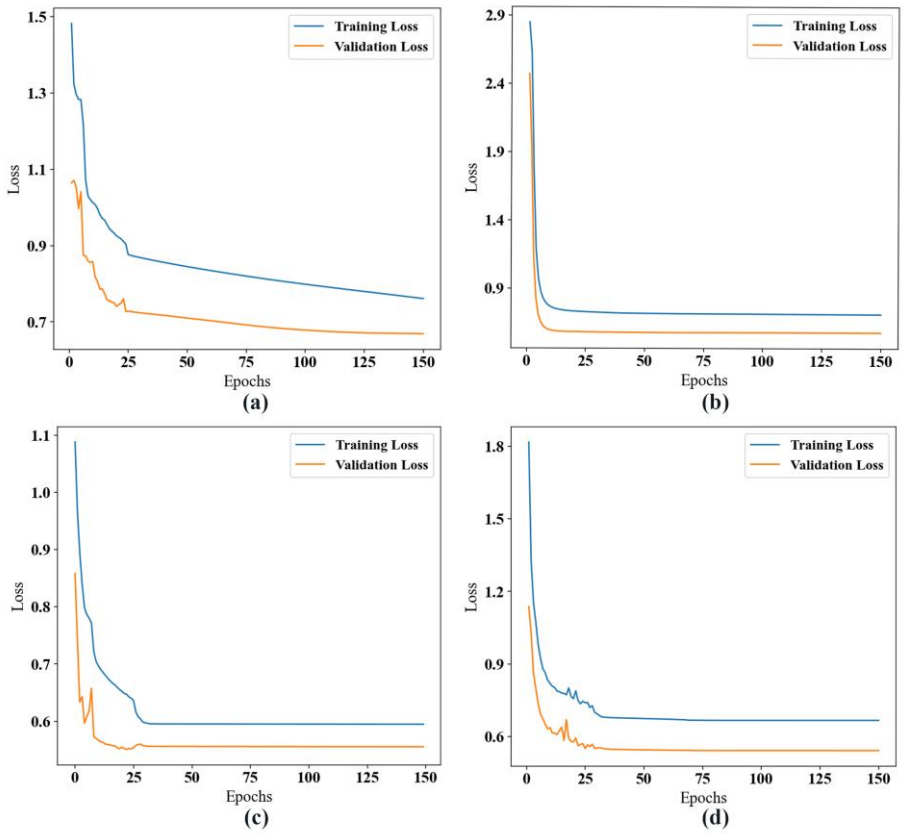

Figure 11. Loss function plots for the four models predicting chlorophyll-a. (**a**) ConvLSTM, (**b**) CNN-LSTM, (**c**) E3D-LSTM, (**d**) SA-ConvLSTM.

The performance of different models in predicting Chl-a in the YBS could be evaluated using Taylor diagrams, which included indicators such as r, centered root mean square, and NSD (Figure 12). The SA-ConvLSTM model performed best in the prediction of Chl-a, with an r of 0.887 and an NSD of 0.962. Following the SA-ConvLSTM, the E3D-LSTM model produced the second-best results, with an r of 0.870 and an NSD of 0.955. ConvLSTM had an r of only 0.851 and an NSD of 0.854, performing the worst among the four models. Therefore, it was concluded that the SA-ConvLSTM model had the best prediction effect for Chl-a in the YBS.

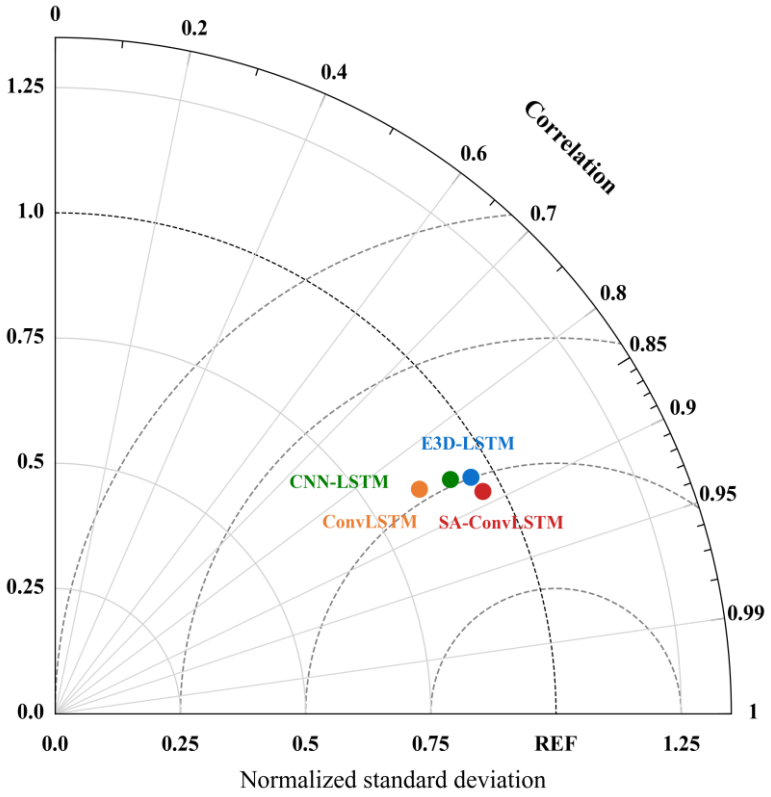

Figure 12. Taylor plot of the model performances in predicting Chl-a on the testing set in the YBS.

According to the above four models, the sea surface Chl-a in the YBS was trained, verified, and tested, and the accuracy results obtained are shown in Table 2.

Table 2. Comparison of chlorophyll-a prediction results in the YBS under four deep learning models.

Period	Deep Learner	r	MAE	MSE	RMSE
Training period	ConvLSTM	0.827	0.250	0.669	0.818
	CNN-LSTM	0.849	0.205	0.580	0.762
	E3D-LSTM	0.860	0.208	0.555	0.745
	SA-ConvLSTM	0.879	0.227	0.540	0.735
Testing period	ConvLSTM	0.851	0.232	0.656	0.810
	CNN-LSTM	0.860	0.218	0.518	0.719
	E3D-LSTM	0.869	0.206	0.495	0.704
	SA-ConvLSTM	0.887	0.212	0.482	0.687

Table 2 illustrates that SA-ConvLSTM exhibited the smallest MSE and RMSE in both training and testing periods and achieved the maximum value of r (r = 0.887, MAE = 0.212 mg/m^3, MSE = 0.482 mg/m^3, RMSE = 0.687 mg/m^3). Therefore, it was considered the optimal model for Chl-a prediction in the YBS. For the ConvLSTM and SA-ConvLSTM, it was shown that the introduction of SAM improved the prediction accuracy by 3.6% by enhancing the capture of long-term spatial information by the model. However, this improvement came at the cost of longer training times due to the increase in model complexity. Compared with the ConvLSTM, the number of parameters of SA-ConvLSTM increased by 0.842 M, and the time required for the model increased by 4.711 s per training round (Table 3). Additionally, the trends of MSE and MAE were not identical as the E3D-LSTM had the smallest MAE (0.206 mg/m^3) in the testing phase but required the longest training time among all four models due to its complex structure. ConvLSTM (r = 0.851) and CNN-LSTM (r = 0.860) showed relatively good prediction performance. ConvLSTM exhibited the lowest number of parameters among the four models, while the CNN-LSTM

model, despite having the highest number of parameters, had the shortest training time required. This could be due to the highly optimized and efficient design of the CNN-LSTM, which enabled it to achieve superior performance with fewer training iterations. Overall, based on the comprehensive evaluation of training time, parameter quantity, and accuracy, SA-ConvLSTM was deemed to be the most effective model for predicting Chl-a in the YBS among the four models.

Table 3. Comparison of model performance of four deep learning models.

Performance Evaluation	ConvLSTM	CNN-LSTM	E3D-LSTM	SA-ConvLSTM
Number of parameters (M)	1.066	328.531	111.709	1.908
Time/Epoch (s)	12.189	8.615	1513.579	16.900

4. Discussion

Large-scale and accurate prediction of Chl-a concentrations is of great significance for preventing large-scale algal blooms and addressing marine environmental pollution. This study considered the relationship between Chl-a and 14 parameters, such as SST, ocean waves, sea breeze, and carbon. Four deep learning models (ConvLSTM, CNN-LSTM, E3D-LSTM, and SA-ConvLSTM) were trained to predict the Chl-a concentrations in the YBS.

Deep learning has significant advantages in dealing with complex data and can automatically learn high-level feature representation from the original dataset. The four models for predicting Chl-a were trained with 14 other features in the dataset except for Chl-a. To verify the rationality of the input data, we calculated the r between the features. Figure 13 presents an analysis of the linear relationship between Chl-a and various characteristics, where the color of each square represents the different r between the two variables. There is a strong linear relationship between Chl-a and PAR (r = 0.64), POC (r = 0.73), NFLH (r = 0.67), T2M (r = 0.60), MSL (r = 0.60), and SP (r = 0.60). Chl-a and U10 (r = 0.13) and V10 (r = −0.12) have weak linear relationships.

In order to evaluate the influence of features not considered in the related studies and input features with weak correlation on the experimental results, we performed ablation experiments. We used eight different input data to put into the best-performing model, SA-ConvLSTM, for training and testing. Table 4 showed that, compared with several other input data, the best experimental results were obtained with 14 features as input data, which can preliminarily verify that our input data were reasonable.

Table 4. SA-ConvLSTM model ablation results in the Yellow Sea and Bohai Sea on the testing set.

Dropped Feature	r	MAE	MSE	RMSE
U10	0.886	0.213	0.487	0.690
V10	0.884	0.215	0.489	0.691
MWD	0.876	0.218	0.554	0.734
MWP	0.877	0.226	0.514	0.709
SWH	0.876	0.209	0.548	0.730
TP	0.876	0.213	0.551	0.733
U10, V10	0.878	0.206	0.542	0.727
MWD, TP, MWP, SWH	0.875	0.211	0.553	0.734
Non-Removal	0.887	0.212	0.482	0.687

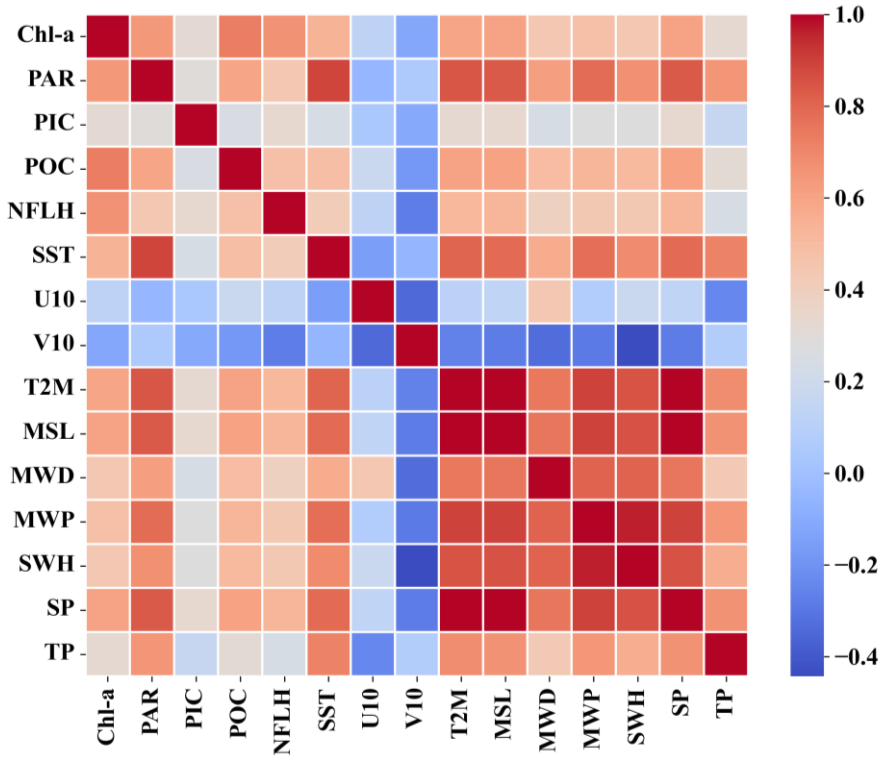

Figure 13. Heatmap for the matrix of Pearson's correlation coefficients.

This work utilized two deep learning models (E3D-LSTM and SA-ConvLSTM) for the first time to predict Chl-a concentrations in the YBS. These models have demonstrated promising performance in prediction accuracy. Additionally, the CNN-LSTM model developed in this study exhibited an advantage in terms of training time. However, training deep learning models requires a large amount of accurate data, and the performance of the models can be affected by missing values. If 8 days of MODIS data are used, the missing rate of the data will be higher relative to the monthly average data. In this study, DINEOF was employed to fill in the missing values, leading to improved results. However, disparities between the imputed data and the actual data persist. Consequently, future research should focus on exploring more accurate and effective methods to enhance the fidelity of satellite data, thereby reducing the disparities with real data. Sea surface Chl-a is influenced by various factors, including vertical sea movements and human activities, which cannot be instantaneously captured by satellite data [57]. Therefore, more data are needed to explore the influencing factors of Chl-a to achieve greater improvement in the prediction effect.

5. Conclusions

In this study, four deep learning models, including ConvLSTM, CNN-LSTM, E3D-LSTM, and SA-ConvLSTM, were used to predict the Chl-a concentrations in the sea surface of the YBS, and the relationship between Chl-a and variables such as SST, POC, SP, wave, and sea wind was comprehensively considered in the prediction of Chl-a by using MODIS and ERA5 remote sensing data. The block training method is used to address the challenge of huge amounts of data requiring significant hardware resources. The results indicated that, compared with the Bohai Sea, the prediction values of the four models for the Chl-a concentrations in the deep sea and the Yellow Sea were closer to the actual Chl-a concentrations. Among the four models, SA-ConvLSTM had the best Chl-a prediction performance for the YBS, with RMSE = 0.687 mg/m^3 and r = 0.887. E3D-LSTM had the best MAE (0.206 mg/m^3). ConvLSTM and CNN-LSTM showed advantages in model training time and were relatively efficient. The introduction of the SAM enhanced the capability of the

SA-ConvLSTM model to capture variations in Chl-a concentrations in the YBS. Compared to the ConvLSTM, the SA-ConvLSTM model exhibited a slight increase of 0.842 M in the number of parameters. However, the introduction of the SAM led to a notable improvement in the prediction accuracy of the model by 3.6%. This study demonstrated the feasibility of using deep learning for sea surface Chl-a prediction in the YBS, providing a reliable method for marine environmental monitoring and analysis.

Author Contributions: L.Y. Data curation, investigation, methodology, software, code, writing—original draft; J.Z. conceptualization, funding acquisition, supervision; writing—review; X.W. software, investigation, visualization, writing—review; X.Y. software, visualization, writing—review; S.Z. code, visualization, writing—review; Q.L. writing—review. All authors have read and agreed to the published version of the manuscript.

Funding: This work was jointly supported by the Central Guiding Local Science and Technology Development Fund of Shandong—Yellow River Basin Collaborative Science and Technology Innovation Special Project (No. YDZX2023019), Shandong Natural Science Foundation of China (No. ZR2017ZB0422, No. ZR2020QE281), the CAS Strategic Priority Research Program (No. XDA19030402), "Taishan Scholar" Project of Shandong Province (No. TSXZ201712).

Data Availability Statement: Not applicable.

Conflicts of Interest: The authors declare no conflict of interest.

References

1. Sammartino, M.; Buongiorno Nardelli, B.; Marullo, S.; Santoleri, R. An Artificial Neural Network to Infer the Mediterranean 3D Chlorophyll-a and Temperature Fields from Remote Sensing Observations. *Remote Sens.* **2020**, *12*, 4123. [CrossRef]
2. Zhao, N.; Zhang, G.; Zhang, S.; Bai, Y.; Ali, S.; Zhang, J. Temporal-Spatial Distribution of Chlorophyll-a and Impacts of Environmental Factors in the Bohai Sea and Yellow Sea. *IEEE Access* **2019**, *7*, 160947–160960. [CrossRef]
3. Xing, M.; Yao, F.; Zhang, J.; Meng, X.; Jiang, L.; Bao, Y. Data reconstruction of daily MODIS chlorophyll-a concentration and spatio-temporal variations in the Northwestern Pacific. *Sci. Total Environ.* **2022**, *843*, 156981. [CrossRef]
4. Wang, Y.; Gao, Z.; Liu, D. Multivariate DINEOF Reconstruction for Creating Long-Term Cloud-Free Chlorophyll-a Data Records From SeaWiFS and MODIS: A Case Study in Bohai and Yellow Seas, China. *IEEE J. Sel. Top. Appl. Earth Obs. Remote Sens.* **2019**, *12*, 1383–1395. [CrossRef]
5. Cullen, J. The Deep Chlorophyll Maximum: Comparing Vertical Profiles of Chlorophyll a. *Can. J. Fish. Aquat. Sci.* **1982**, *39*, 791–803. [CrossRef]
6. Fu, Y.; Xu, S.-g.; Liu, J. Temporal-spatial variations and developing trends of Chlorophyll-a in the Bohai Sea, China. *Estuar. Coast. Shelf Sci.* **2016**, *173*, 49–56. [CrossRef]
7. Lu, X.; Liu, C.; Niu, Y.; Yu, S.X. Long-term and regional variability of phytoplankton biomass and its physical oceanographic parameters in the Yellow Sea, China. *Estuar. Coast. Shelf Sci.* **2021**, *260*, 107497. [CrossRef]
8. Andersen, J.H.; Schlüter, L.; Ærtebjerg, G. Coastal eutrophication: Recent developments in definitions and implications for monitoring strategies. *J. Plankton Res.* **2006**, *28*, 621–628. [CrossRef]
9. Cho, H.; Choi, U.J.; Park, H. Deep Learning Application to Time Series Prediction of Daily Chlorophyll-a Concentration. *WIT Trans. Ecol. Environ.* **2018**, *215*, 157–163.
10. Barzegar, R.; Aalami, M.T.; Adamowski, J. Short-term water quality variable prediction using a hybrid CNN–LSTM deep learning model. *Stoch. Environ. Res. Risk Assess.* **2020**, *34*, 415–433. [CrossRef]
11. Xiao, X.; He, J.; Huang, H.; Miller, T.R.; Christakos, G.; Reichwaldt, E.S.; Ghadouani, A.; Lin, S.; Xu, X.; Shi, J. A novel single-parameter approach for forecasting algal blooms. *Water Res.* **2017**, *108*, 222–231. [CrossRef]
12. Li, X.; Sha, J.; Wang, Z.L. Application of feature selection and regression models for chlorophyll-a prediction in a shallow lake. *Environ. Sci. Pollut. Res. Int.* **2018**, *25*, 19488–19498. [CrossRef] [PubMed]
13. Kiyomoto, Y.; Iseki, K.; Okamura, K. Ocean Color Satellite Imagery and Shipboard Measurements of Chlorophyll a and Suspended Particulate Matter Distribution in the East China Sea. *J. Oceanogr.* **2001**, *57*, 37–45. [CrossRef]
14. Ndungu, J.; Monger, B.C.; Augustijn, D.C.M.; Hulscher, S.J.M.H.; Kitaka, N.; Mathooko, J.M. Evaluation of spatio-temporal variations in chlorophyll-a in Lake Naivasha, Kenya: Remote-sensing approach. *Int. J. Remote Sens.* **2013**, *34*, 8142–8155. [CrossRef]
15. Cui, T.; Zhang, J.; Tang, J.; Sathyendranath, S.; Groom, S.; Ma, Y.; Zhao, W.; Song, Q. Assessment of satellite ocean color products of MERIS, MODIS and SeaWiFS along the East China Coast (in the Yellow Sea and East China Sea). *ISPRS J. Photogramm. Remote Sens.* **2014**, *87*, 137–151. [CrossRef]
16. Meng, X.; Yao, F.; Zhang, J.; Liu, Q.; Liu, Q.; Shi, L.; Zhang, D. Impact of dust deposition on phytoplankton biomass in the Northwestern Pacific: A long-term study from 1998 to 2020. *Sci. Total Environ.* **2022**, *813*, 152536. [CrossRef]

17. Vollenweider, R.A. Input-Output Models with Special Reference to the Phosphorus Loading Concept in Limnology. *Schweiz. Z. Für Hydrol.* **1975**, *37*, 53–84. [CrossRef]
18. Jørgensen, S.E.; Mejer, H.; Friis, M. Examination of a lake model. *Ecol. Model.* **1978**, *4*, 253–278. [CrossRef]
19. Box, G.E.P.; Jenkins, G.M.; Reinsel, G.C. *Time Series Analysis: Forecasting and Control*, 3rd ed.; Prentice Hall: Eng-lewood Cliffs, NJ, USA, 1994.
20. Xiao, C.; Chen, N.; Hu, C.; Wang, K.; Xu, Z.; Cai, Y.; Xu, L.; Chen, Z.; Gong, J. A spatiotemporal deep learning model for sea surface temperature field prediction using time-series satellite data. *Environ. Model. Softw.* **2019**, *120*, 104502. [CrossRef]
21. Zhou, S.; Xie, W.; Lu, Y.; Wang, Y.; Zhou, Y.; Hui, N.; Dong, C. ConvLSTM-Based Wave Forecasts in the South and East China Seas. *Front. Mar. Sci.* **2021**, *8*, 740. [CrossRef]
22. Na, L.; Shaoyang, C.; Zhenyan, C.; Xing, W.; Yun, X.; Li, X.; Yanwei, G.; Tingting, W.; Xuefeng, Z.; Siqi, L. Long-term prediction of sea surface chlorophyll-a concentration based on the combination of spatio-temporal features. *Water Res.* **2022**, *211*, 118040. [CrossRef] [PubMed]
23. Yu, B.; Xu, L.; Peng, J.; Hu, Z.; Wong, A. Global chlorophyll-a concentration estimation from moderate resolution imaging spectroradiometer using convolutional neural networks. *J. Appl. Remote Sens.* **2020**, *14*, 034520. [CrossRef]
24. Yussof, F.N.; Maan, N.; Md Reba, M.N. LSTM Networks to Improve the Prediction of Harmful Algal Blooms in the West Coast of Sabah. *Int. J. Environ. Res. Public Health* **2021**, *18*, 7650. [CrossRef]
25. Ham, Y.-G.; Kim, J.-H.; Luo, J.-J. Deep learning for multi-year ENSO forecasts. *Nature* **2019**, *573*, 568–572. [CrossRef] [PubMed]
26. Ahmed, M.; Mumtaz, R.; Anwar, Z.; Shaukat, A.; Arif, O.; Shafait, F. A Multi–Step Approach for Optically Active and Inactive Water Quality Parameter Estimation Using Deep Learning and Remote Sensing. *Water* **2022**, *14*, 2112. [CrossRef]
27. Shi, X.; Chen, Z.; Wang, H.; Yeung, D.Y.; Wong, W.K.; Woo, W.C. *Convolutional LSTM Network: A Machine Learning Approach for Precipitation Nowcasting*; MIT Press: Cambridge, MA, USA, 2015.
28. Wang, Y.; Long, M.; Wang, J.; Gao, Z.; Philip, S.Y. PredRNN: Recurrent neural networks for predictive learning using spatiotemporal LSTMs. In Proceedings of the Advances in Neural Information Processing Systems, Long Beach, CA, USA, 4–9 December 2017; pp. 879–888.
29. Wang, Y.; Gao, Z.; Long, M.; Wang, J.; Yu, P.S. PredRNN++: Towards a Resolution of the Deep-in-Time Dilemma in Spatiotemporal Predictive Learning. In Proceedings of the 35th International Conference on Machine Learning, ICML 2018, Stockholm, Sweden, 15 July 2018; Volume 11, pp. 8122–8131.
30. Wang, Y.; Lu, J.; Ming, H.Y.; Li, J.L.; Long, M.; Fei-Fei, L. Eidetic 3D LSTM: A Model for Video Prediction and Beyond. In Proceedings of the International Conference on Learning Representations, New Orleans, LA, USA, 6–9 May 2019.
31. Lin, Z.; Li, M.; Zheng, Z.; Cheng, Y.; Yuan, C. Self-Attention Convlstm for Spatiotemporal Prediction. In Proceedings of the AAAI Conference on Artificial Intelligence, New York, NY, USA, 7–12 February 2020; The AAAI Press: Palo Alto, CA, USA, 2020; Volume 34, pp. 11531–11538.
32. Luo, C.; Zhao, X.; Sun, Y.; Li, X.; Ye, Y. PredRANN: The spatiotemporal attention Convolution Recurrent Neural Network for precipitation nowcasting. *Knowl.-Based Syst.* **2022**, *239*, 107–109. [CrossRef]
33. Wang, Y.; Wu, J.; Long, M.; Tenenbaum, J.B. Probabilistic Video Prediction From Noisy Data With a Posterior Confidence. In Proceedings of the 2020 IEEE/CVF Conference on Computer Vision and Pattern Recognition (CVPR), Seattle, WA, USA, 13–19 June 2020; pp. 10827–10836.
34. Wu, H.; Yao, Z.; Long, M.; Wan, J. MotionRNN: A Flexible Model for Video Prediction with Spacetime-Varying Motions. In Proceedings of the 2021 IEEE/CVF Conference on Computer Vision and Pattern Recognition (CVPR), Nashville, TN, USA, 20–25 June 2021; pp. 15430–15439.
35. Wang, Y.; Wu, H.; Zhang, J.; Gao, Z.; Wang, J.; Yu, P.S.; Long, M. PredRNN: A Recurrent Neural Network for Spatiotemporal Predictive Learning. *IEEE Trans. Pattern Anal. Mach. Intell.* **2021**, *45*, 2208–2225. [CrossRef]
36. Natural Earth. Available online: https://www.naturalearthdata.com (accessed on 25 August 2023).
37. OceanColor. Available online: https://oceancolor.gsfc.nasa.gov (accessed on 29 March 2022).
38. Luo, X.; Song, J.; Guo, J.; Fu, Y.; Wang, L.; Cai, Y. Reconstruction of chlorophyll-a satellite data in Bohai and Yellow sea based on DINCAE method. *Int. J. Remote Sens.* **2022**, *43*, 3336–3358. [CrossRef]
39. Zhai, F.; Wu, W.; Gu, Y.; Li, P.; Song, X.; Liu, P.; Liu, Z.; Chen, Y.; He, J. Interannual-decadal variation in satellite-derived surface chlorophyll-a concentration in the Bohai Sea over the past 16 years. *J. Mar. Syst.* **2020**, *215*, 103496. [CrossRef]
40. Volpe, G.; Nardelli, B.B.; Cipollini, P.; Santoleri, R.; Robinson, I.S. Seasonal to interannual phytoplankton response to physical processes in the Mediterranean Sea from satellite observations. *Remote Sens. Environ.* **2012**, *117*, 223–235. [CrossRef]
41. Behrenfeld, M.J.; Falkowski, P.G. Photosynthetic rates derived from satellite-based chlorophyll concentration. *Limnol. Oceanogr.* **1997**, *42*, 1–20. [CrossRef]
42. Gong, G.-C.; Liu, K.-K. The Relationship Between Surface Chlorophyll a and Biogenic Matter in the Euphotic Zone in the Southern East China Sea in Spring. *COSPAR Colloquia Ser.* **1997**, *8*, 175–178.
43. Gupta, G.V.M.; Sudheesh, V.; Sudharma, K.V.; Saravanane, N.; Dhanya, V.; Dhanya, K.R.; Lakshmi, G.; Sudhakar, M.; Naqvi, S.W.A. Evolution to decay of upwelling and associated biogeochemistry over the southeastern Arabian Sea shelf. *J. Geophys. Res. Biogeosciences* **2016**, *121*, 159–175. [CrossRef]
44. Liang, Z.; Soranno, P.A.; Wagner, T. The role of phosphorus and nitrogen on chlorophyll a: Evidence from hundreds of lakes. *Water Res.* **2020**, *185*, 116236. [CrossRef]

45. Beckers, J.M.; Barth, A.; Alvera-Azcárate, A. DINEOF reconstruction of clouded images including error maps. Application to the Sea-Surface Temperature around Corsican Island. *Ocean Sci.* **2006**, *2*, 183–199. [CrossRef]
46. Prasetyowati, S.A.D.; Ismail, M.; Budisusila, E.N.; Setiadi, D.R.I.M.; Purnomo, M.H. Dataset Feasibility Analysis Method based on Enhanced Adaptive LMS method with Min-max Normalization and Fuzzy Intuitive Sets. *Int. J. Electr. Eng. Inform.* **2022**, *14*, 55–75. [CrossRef]
47. Szegedy, C.; Liu, W.; Jia, Y.; Sermanet, P.; Reed, S.; Anguelov, D.; Erhan, D.; Vanhoucke, V.; Rabinovich, A. Going deeper with convolutions. In Proceedings of the IEEE Conference on Computer Vision and Pattern Recognition, Boston, MA, USA, 7–12 June 2015; pp. 1–9.
48. Nogueira, K.; Penatti, O.; Santos, J. Towards Better Exploiting Convolutional Neural Networks for Remote Sensing Scene Classification. *Pattern Recognit.* **2016**, *61*, 539–556. [CrossRef]
49. Vaswani, A.; Shazeer, N.; Parmar, N.; Uszkoreit, J.; Jones, L.; Gomez, A.N.; Kaiser, L.; Polosukhin, I. Attention Is All You Need. In Proceedings of the Advances in Neural Information Processing Systems 30, Long Beach, CA, USA, 4–9 December 2017; pp. 5998–6008.
50. Ge, H.; Li, S.; Cheng, R.; Chen, Z. Self-Attention ConvLSTM for Spatiotemporal Forecasting of Short-Term Online Car-Hailing Demand. *Sustainability* **2022**, *14*, 7371. [CrossRef]
51. Jacobs, R.A. Increased Rates of Convergence Through Learning Rate Adaptation. *Neural Netw.* **1988**, *1*, 295–307. [CrossRef]
52. Donahue, J.; Hendricks, L.A.; Rohrbach, M.; Venugopalan, S.; Guadarrama, S.; Saenko, K.; Darrell, T. Long-Term Recurrent Convolutional Networks for Visual Recognition and Description. *IEEE Trans. Pattern Anal. Mach. Intell.* **2017**, *39*, 677–691. [CrossRef]
53. Nair, V.; Hinton, G.E. Rectified Linear Units Improve Restricted Boltzmann Machines. In Proceedings of the 27th International Conference on Machine Learning (ICML-10), Haifa, Israel, 21–24 June 2010; pp. 807–814.
54. Girosi, F.; Jones, M.; Poggio, T. Regularization Theory and Neural Networks Architectures. *Neural Comp.* **1995**, *7*, 219–269. [CrossRef]
55. Ghorbani, M.A.; Deo, R.C.; Karimi, V.; Yaseen, Z.M.; Terzi, O. Implementation of a hybrid MLP-FFA model for water level prediction of Lake Egirdir, Turkey. *Stoch. Environ. Res. Risk Assess.* **2018**, *32*, 1683–1697. [CrossRef]
56. Paerl, H.; Otten, T. Harmful Cyanobacterial Blooms: Causes, Consequences, and Controls. *Microb. Ecol.* **2013**, *65*, 995–1010. [CrossRef] [PubMed]
57. Zhang, H.; Qiu, Z.; Sun, D.; Wang, S.; He, Y. Seasonal and Interannual Variability of Satellite-Derived Chlorophyll-a (2000–2012) in the Bohai Sea, China. *Remote Sens.* **2017**, *9*, 582. [CrossRef]